PCCP

Intermetallic alloy structure-activity descriptors derived from inelastic X-ray scattering

SCHOLARONE™
Manuscripts

Intermetallic alloy structure-activity descriptors derived from inelastic X-ray scattering

Brandon C. Bukowski[1‡], Stephen C. Purdy[1‡], Evan C. Wegener[1], Zhenwei Wu[1], A. Jeremy Kropf[2], Guanghui Zhang[1,3], Jeffrey T. Miller[1]*, Jeffrey Greeley[1]*

[1]Charles D. Davidson School of Chemical Engineering, Purdue University, 480 Stadium Mall Drive, West Lafayette, Indiana 47907, United States.

[2]Chemical Sciences and Engineering Division, Argonne National Laboratory, 9700 South Cass Avenue, Argonne, Illinois 60439, United States.

[3]State Key Laboratory of Fine Chemicals, PSU-DUT Joint Center for Energy Research, School of Chemical Engineering, Dalian University of Technology, Dalian, Liaoning 116024, PR China.

Abstract Synchrotron spectroscopy and density functional theory (DFT) are combined to develop a new descriptor for the stability of adsorbed chemical intermediates on metal alloy surfaces. This descriptor probes the separation of occupied and unoccupied d electron density in platinum and is related to shifts in Resonant Inelastic X-ray Scattering (RIXS) signals. Simulated and experimental spectroscopy are directly compared to show that the promoter metal identity controls the orbital shifts in platinum electronic structure. The associated RIXS features are correlated with the differences in the band centers of the occupied and unoccupied d bands, providing chemical intuition for the alloy ligand effect and providing a connection to traditional descriptions of chemisorption. The ready accessibility of this descriptor to both DFT calculations and experimental spectroscopy, and its connection to chemisorption, allow for deeper connections between theory and characterization in the discovery of new catalysts.

Introduction

Intermetallic alloys with crystallographically distributed metal atoms are a promising subset of heterogeneous catalysts to investigate the electronic structure modification of active sites. For example, platinum electron bands have been tuned by synthesizing subsurface transition metal alloys,[1–3] dilute single site alloys,[4–6] and polycrystalline alloys[7,8] for more reactive and selective catalytic conversions. The well-defined active sites of intermetallics[9–12] are amenable to computational studies that distinguish electronic structure changes. Platinum intermetallic alloys with various 3d metals have been reported in the literature,[10] in particular Pt_3Ti and Pt_3V,[13,14] Pt_3Cr,[15] Pt_3Mn,[16] $PtZn$,[17,18] and $PtFe$,[19] among others[20]. Many of these catalysts are relevant for chemistries such as dehydrogenation,[20–22] hydrogenation,[23–25] and methanation.[26,27] Dehydrogenation to produce olefins is of particular interest as the availability of shale gas has driven interest in new technologies to produce fuels and valuable chemicals from low molecular weight alkanes such as methane, ethane, and propane[28,29] using catalysis. While intermetallics are of interest for heterogeneous catalysis, there is no unified chemical model to predict how modification of the Pt electronic structure affects reactivity and selectivity.

Many features of alloy catalysts were introduced by Sinfelt, Carter, and Yates who showed that alloying nickel with copper breaks up nickel ensembles, reducing the rate of hydrogenolysis without changing the rate of dehydrogenation.[30,31] The sensitivity of heterogeneous reactions to catalyst surface structure has been used to control catalyst selectivity by preventing unselective C-C bond cleavage with different promoter metals and structures[32] that are also implicated in deactivation mechanisms.[33] For example, the geometric effects of Sn incorporation in Pt-Sn catalysts have been the topic of much interest experimentally[34–36] and with Density Functional Theory (DFT).[37,38] Previous reports have shown that electronic effects in alloys can manifest through a variety of functions including ligand effects, strain, and charge transfer[39–41] making a combination of investigative techniques necessary to determine the dominant effect of the promoter metal.

One of the most successful models to correlate electronic structure and chemisorption on catalytic surfaces is the d-band model developed by Hammer and Nørskov.[42–45] The d-band model approximates the Newns-Anderson model[46] that relates the adsorption energies of reactive intermediates to the density of metal d electron states. This model has been widely used to understand the alloying effect of subsurface promoter metals[1] and intermetallic compounds.[47] Physical measurement of d bands require ultraviolet photoemission spectroscopy[7] (UPS) or high resolution X-ray photoelectron spectroscopy[48] (XPS) on single crystals in ultrahigh vacuum (UHV). However, a new spectroscopic technique, resonant inelastic X-ray scattering[49–51] (RIXS), has been applied to transition metal nanoparticles,[52,53] solvated organometallic complexes,[54] and Fe ions in the oxyhemoglobin protein[55] to interpret shifts in metal valence band d states. We have previously reported on the electronic shift of valence orbitals for platinum alloyed with Zn,[18] as well as varying compositions of intermetallic PtFe alloys.[19] We and others have previously reported on computational approaches to model RIXS[18,19,52] that show the spectroscopy can be directly compared with simulations. RIXS can therefore directly link experimental signatures with simulations to

directly describe the electronic effect of alloy formation in heterogeneous catalysis.

In this work, we compare RIXS spectroscopy signatures for a family of platinum intermetallics to highlight how promoter identity tunes Pt electronic structure. These experiments provide direct evidence that the separation of Pt bands is due to electronic interactions between Pt and the promoter. DFT simulations are quantitatively compared to the experimentally measured chemical shifts and provide physical intuition to promoter effects. We find that the RIXS energy transfer directly correlates with the separation in the occupied and unoccupied d-band densities of state of platinum. The Pt d states are still continuous across the Fermi level, but the occupied and unoccupied states have peaked distributions. Armed with this intuition, we propose the use of the RIXS energy transfer as a descriptor for carbon adsorption, which is closely related to product selectivity for a variety of alkane chemistries, on bimetallic surfaces. We conclude that alloys with larger Pt band separation destabilize unsaturated carbon intermediates to a greater degree than for more saturated carbon intermediates, providing a fundamental electronic structure-based description of selectivity trends in alkane chemistry on transition metal surfaces.

Methods
RIXS

RIXS spectra were collected on the MRCAT insertion device (10ID) line of the Advanced Photon Source, Argonne National Laboratory. The silica supported catalyst was ground to a fine powder and pressed into a self-supporting wafer inside of a stainless steel sample holder. Sample treatment was performed in a purpose-built in-situ cell capable of heating and gas flow, described elsewhere[62]. Collection of transmission X-ray absorption and fluorescent X-ray Emission spectra was made possible by three kapton windows in the cell. Samples were reduced at 550°C in 3.5% H_2 (balance He) for 30 minutes and then cooled to 100°C in 3.5% H_2 (balance He) for measurement.

Prior to measurements, the monochromator energy was calibrated using platinum foil, with an edge energy of 11562.76 eV[63]; a foil spectrum was also recorded simultaneously with each sample using a third ion chamber. During RIXS measurements, the X-ray beam was microfocused using a set of Kirkpatric-Baez mirrors. X-ray Absorption at the Pt L_3 edge was measured using a set of ion chambers, with uncertainties in the incident photon energies estimated to be ~0.1-0.2 eV. The $L\beta_5$ (L_3-$O_{4,5}$) X-ray emission line was measured using a bent crystal spectrometer[64]. The wavelength dispersive spectrometer was based on a bent silicon crystal. Fluoresced X-rays were detected using a Pilatus 100K (Dectris) 2D pixel array detector. The analyzer crystal used was a 55-μm thick Si (400) wafer cylindrically bent with an approximate bend radius of 0.5 m. X-rays were scattered from the Si(133) plane with a calculated asymmetry angle of 13.76°. The crystal analyzer was declined 20° from the sample horizontal to allow enough elastically scattered X-rays through the analyzer that the fluorescence energy scale could be calibrated based on the elastic scattering peak position. The intensity of the elastically scattered peak was approximately 5 times that of the inelastic scattering peak. RIXS maps were then plotted as fluorescence intensity maps as a function of incident photon energy (abssica) and emission energy relative to the elastic scattering peak (ordinate), hereafter termed energy transfer, with the elastic scattering maximum corresponding to 0 energy transfer. The elastic scattering peak was subtracted from the RIXS maps by fitting a Gaussian curve to the truncated data, using a fixed value for the full width at half maximum (FWHM) and peak position per sample, and a linearly varying amplitude with incident photon energy to account for beam polarization changing the elastic scattering amplitude as a function of emission angle. The emission intensity scale was normalized per sample relative to the maximum intensity point of the inelastic scattering peak. Inelastic peak centroids were found by fitting a 2D quadratic function about a 2eV by 2eV fit window centered at the maximum intensity position using the centroids utility in the Phototutils phyton package.[65] This localized fitting approach gave centroid values least sensitive to the non-resonant tail of the RIXS plane, which was more pronounced for samples with higher Pt loading.

Density Functional Theory Calculations

Density Functional Theory (DFT) calculations were performed using the Vienna Ab Initio Simulation Package (VASP)[66–69] using the Projector Augmented Wave pseudopotentials[70,71]. The PBE exchange and correlation functional[72], which has been extensively benchmarked for the treatment of metals was used for all calculations[73]. Lattice constants for pure Pt, as well as each of the alloys were optimized using a 600 eV energy cutoff, a 10x10x10 gamma centered k point grid, and Methfessel-Paxton smearing. Lattice constants were converged to a force criterion of 20 meV / Å. All calculations are performed spin-polarized with initial magnetic moments specified to ensure the magnetic moments correspond to the lowest energy structure. Converged lattice constants for the full suite of alloys is provided in the S.4.3.

Surface slabs were cut from each bulk according to their closest packed termination. For all Pt_3X compositions a (111) surface was chosen based on the FCC structure of each bulk. PtZn has a body centered tetragonal unit cell, in which the (011) surface has the highest packing density and is chosen for modeling. All surfaces used were 2x2 surface atoms, and 5 layers with 10 Å of vacuum. The bottom 2 layers were constrained to mimic an underlying bulk, while the top 3 layers could relax to a force criterion of 20 meV / Å. The dipole parallel to the vacuum was corrected. A 7x7x1 Gamma centered k point grid was used with Methfessel-Paxton smearing.

The Density of States (DOS) for bulk and surfaces were calculated using the standard VASP projectors. For bulk, the DOS of each Pt atom was averaged along with the up and down spin channel. For surface slabs, only the topmost Pt atoms were averaged along with their up and down spin channels. For bulk, the DOS was calculated using a denser k-point grid of 15x15x15. For surfaces, 15x15x1 k point grids were used.

Moments about the d-band were performed by first normalizing the total density and shifting the Fermi level to 0. All moments were calculated with an upper cutoff of +5 eV above the Fermi energy, to neglect contributions from small but nonzero densities at higher energies beyond the d-band. To account for particle size effects, the relative number of surface and bulk metal atoms was estimated using the relation D ~ 0.9/d where D is the dispersion

expressed as the ration of surface to bulk atoms, and d is the particle size in nm, was used and a weighted average of bulk and surface Pt atoms was constructed for a given particle size[74].

Adsorption of model compounds was performed at the same level of theory as DOS calculations to provide a consistent comparison between electronic structure and adsorption energy. Adsorption energies of each CH_x intermediate is referenced to a stoichiometric balance of methane and molecular hydrogen according to the following relation:

$$E_{ads} = (E_{CHx*} + \frac{(4-x)}{2}E_{H_2(g)}) - (E_* + E_{CH_4(g)}) \quad \text{(eq 2)}$$

Where x denotes the number of hydrogens in the adsorbate molecule. Gas phase calculations were performed in a 8 Å by 9 Å by 10 Å periodic box with a cutoff energy of 450 eV, a single gamma k-point and the same force convergence criteria as used for the bulk.

RIXS Modeling Calculations

RIXS energy planes were calculated using the d-projected DOS (from here denoted as pDOS). The general expression used has been used previously[18,49,52] and is shown in equation 3:

$$F(\Omega,\omega) = \int_{-\infty}^{0} d\varepsilon \frac{\rho_d(\varepsilon)\rho_d{}'(\varepsilon + \Omega - \omega)}{(\varepsilon - \omega)^2 + \frac{\Gamma_n^2}{4}} \quad \text{(eq 3)}$$

Where F is the emitted intensity expressed in terms of the incident energy Ω, and the emission energy ω. The energy transferred is expressed as $\Delta E = \Omega - \omega$. The pDOS of the occupied (below the Fermi level) and unoccupied (above the Fermi level) are ρ_d and $\rho_d{}'$. The broadening of the core hole, Γ_n is taken to be 5.41 eV[37]. The energy of a given state is ε, which is used as an integration index. For each Ω and ω, the range of accessible states in the second term of the numerator implicitly changes the range of the integral, while each specific emission energy ω shifts the range at which spectral broadening is apparent. Effectively, the intensity is a convolution of the occupied and unoccupied d-states governed by the constraints imposed by the incident and emitted energy for accessible transitions broadened by the core hole. The integral was solved on a grid ranging from -4 eV to 10 eV relative to the Fermi energy in Ω, and 0 to 14 eV in ΔE. This was solved using a code written in Python. High intensity peak identification was performed differently than we have reported before. Instead of reporting the point of highest intensity, a 2-D Gaussian function is fitted to the entire high intensity region to extract a mean value. This is less sensitive to sharp details in the DOS which cause non-uniform fluctuations in the broad high-intensity RIXS peak. For a more detailed discussion see S.2.6.

Results and Discussion

The particle size, phase composition, and phase purity of Pt_3V, Pt_3Mn, Pt_3Fe, Pt_3Co, and Pt_3In, have been described previously.[14,16,19,56,57] The Pt L_3 edge X-ray absorption near edge structure (XANES) and L_3-$O_{4,5}$ RIXS planes for PtZn and Pt_3V are reproduced from references [18] and [14] respectively, with some improvements in RIXS data reduction described in the methods section. The Pt-Ga catalyst was determined to be Pt_3Ga, with details of the

characterization given in Supplementary Information section S.2.1.

RIXS plots of Pt, Pt_3V, Pt_3Mn, Pt_3Co, Pt_3In and Pt_3Ga nanoparticles are shown in Figure 1. RIXS maps are plotted as intensity maps as a function of the incident photon
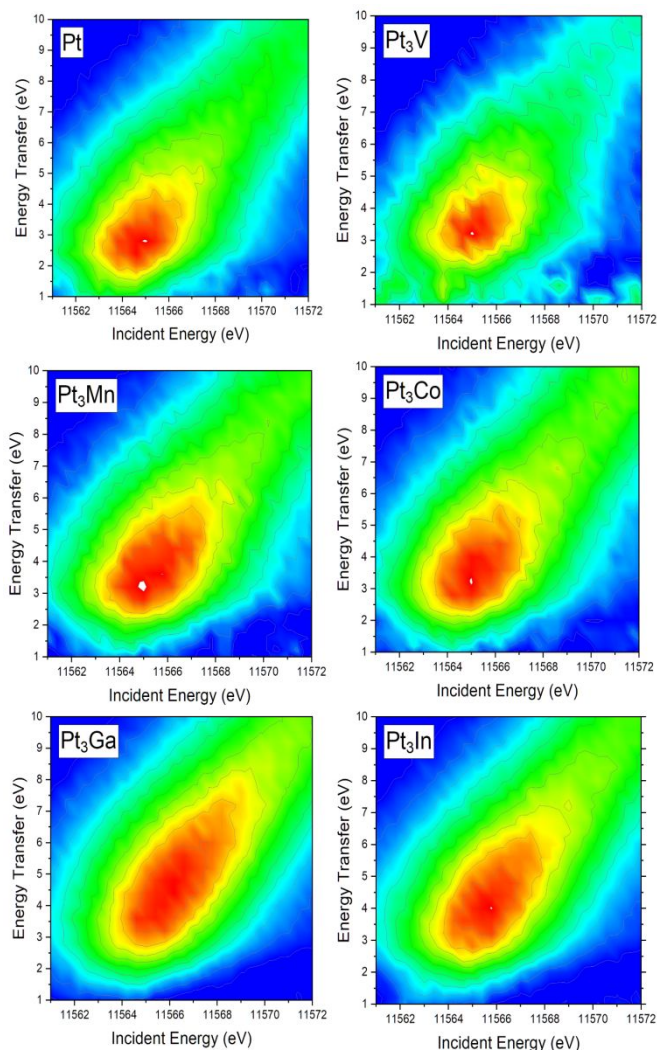
Figure 1: RIXS plots of Pt and Pt alloy catalysts after reduction at 550°C in 3.5% H_2.

energy on the horizontal axis, and the fluoresced photon energy relative to the elastic scattering energy, termed energy transfer, on the vertical axis. The plotted intensity is that of the fluoresced X-rays resulting from scattering. Elastic scattering occurs when the excited $2p_{3/2}$ electron decays back into its own core hole. Inelastic scattering occurs when an electron other than the excited $2p_{3/2}$ electron decays back into the core hole. For the alloy samples, energy transfer maxima are reported for Pt alloys with V, Mn, Fe, Co, Ga, In, Fe, and Zn (Table 1); results for alloys with Cu and Sn, however, are not included, since these alloys could not be made ordered and phase pure with our synthesis procedures, thus complicating direct comparisons with theory. The energy transfer maxima are seen to be shifted to higher values, meaning the energies of both the filled and unfilled states further separate in the alloys while still maintaining metallic character. The shape of the inelastic scattering peak also changes, which reflects the changing distribution of energy states in each alloy

phase. As the incident photon energy increases past the L_3 absorption edge, the resonant enhancement of the $L\beta_5$ fluorescence mode decays and non-resonant scattering leads to a low intensity tail which increases in energy transfer with incident photon energy.

Table 1: Energy transfer maximum values and Pt L_3 edge XANES edge energies for Pt and Pt alloy phases.

Phase	Energy Transfer (eV)	XANES Edge Energy (eV)
Pt	2.8	11562.76
Pt$_3$V	3.3	11563.3
Pt$_3$Mn	3.4	11563.1
Pt$_3$Fe	3.4	11563.0
Pt$_3$Co	3.4	11563.4
Pt$_3$Ga	4.3	11563.6
Pt$_3$In	4.0	11563.6
PtFe[19]	3.6	11563.2
PtFe$_3$[19]	3.9	11563.4
PtZn[18]	4.4	11563.6

The energy transfer values for the platinum alloys with post transition metals (In, Ga, Zn) are larger than those alloys with 3d elements. This is even true for Pt$_3$In and Pt$_3$Ga alloys, where Pt has the same number of Pt-to-promoter bonds as in the other Pt$_3$M alloys measured. For the Pt alloys with 3d metals, however, all measured materials have similar energy transfer values. In all cases, the energy transfer relative to platinum is larger in magnitude than the difference in XANES edge energy relative to platinum, demonstrating that in all structures the average energy of the 5d filled states decreases in energy as the energy of the XANES increases.

The RIXS measurements indicate that not only do Pt d energies shift upon alloy formation, but the magnitude of these shifts depends on the choice of promoter metal. RIXS features provide limited chemical intuition about what to expect for adsorption onto each alloy, and consequently their catalytic properties. Linking RIXS to chemisorption would permit development of a RIXS-based descriptor for surface chemistry that would, in turn, introduce an experimentally accessible electronic structure screening tool for catalyst reactivity. DFT simulations are a powerful tool for relating chemisorption to electronic properties, and DFT can also simulate RIXS spectra. We will first show that DFT can describe the experimental RIXS shifts, and we will then exploit the computational results to develop a descriptor for adsorption based on the RIXS energy transfer that can, in turn, be experimentally measured.

The d-DOS across a range of metal promoters (the full range of 12 promoters available in S.3.4) is shown in Figure 2. Nanoparticle dispersions were approximated by averaging bulk and surface atoms as described in S.2.4. Platinum d-DOS with half-filled d band promoters, such as Mn and Co, form intermetallic alloys with Pt that have a broader range in occupied d states than early transition metals such as V or late transition metals such as Cu. The half d-filled promoters do not significantly shift the Pt d-band center relative to Pt (-0.07 eV and 0.07 eV for Pt in

Pt$_3$Mn and Pt$_3$Co) showing a similar electronic structure for pure Pt and Pt alloyed with half-filled d-band promoters.

Pt$_3$Mn has a unique feature at ~2 eV above the Fermi energy distinct from Pt with relative position insensitive to particle dispersion. A similar, though smaller peak is observed for Pt$_3$Cu closer to ~2.5 eV. These higher energy unoccupied states are not unique to the half-filled d promoters but observed for all alloys at varying position in intensity. In the case of Pt in Pt$_3$V, Pt$_3$Ga, and Pt$_3$Sn; the peak intensity and position changes with particle dispersion, indicating chemical interactions with surface Pt atoms that are dependent on promoter choice. Finally, we note that the strongly peaked distributions of Pt$_3$V, Pt$_3$Ga, and Pt$_3$Sn have
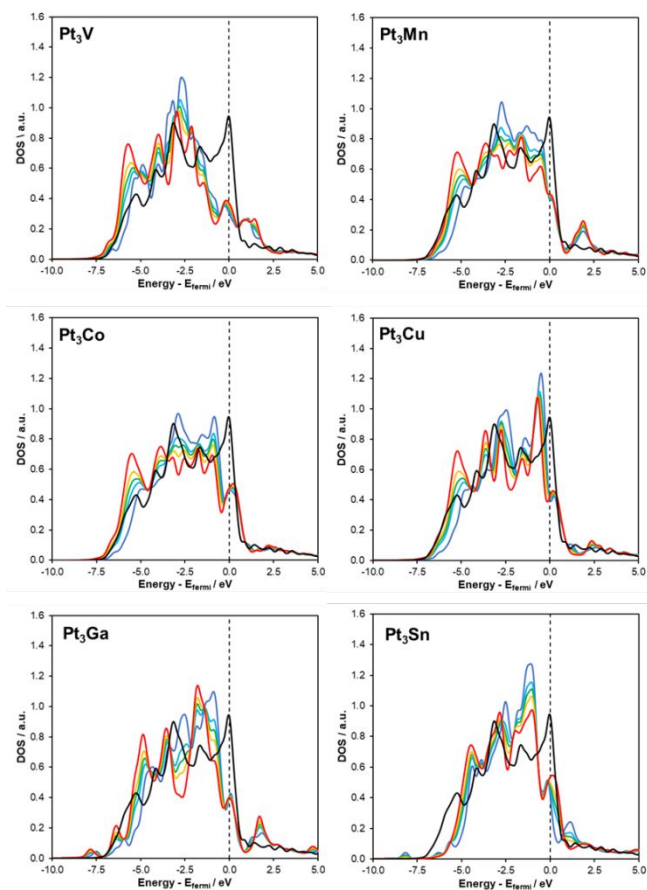
Figure 2. Projected density of state (DOS) of Pt bulk and surface atoms in intermetallic alloys. The DOS are plotted for increasing dispersion from 0% (red), 30% (yellow), 45% (green), 60% (cyan), and 100% (blue). Pure Pt is shown in black. The 6 other intermetallics considered can be found in the Supplementary information S.3.4.

larger d-band center shifts (-0.29 eV, 0.14 eV, 0.14 eV) as compared to pure Pt, reflecting the perturbation in Pt density of states by electronic interaction with promoter metals, as the geometry of each surface (except for PtZn) is dominated by (111) facets. We have found these shifts to not be the result of fractional charge effects or strain effects on the Pt lattice, as discussed in S.2.5.

From dispersion corrected DOS plots, simulated RIXS plots were constructed to evaluate the accuracy to which shifts in the high intensity peak can be described by simulated DOS across the range of 12 promoters. RIXS peaks were fitted to a 2-D Gaussian function as described in

S.2.6. To facilitate the comparison between Pt in simulated alloys as compared to simulated pure Pt, Figure 3 is arranged to show difference RIXS plots for the same subset of intermetallics as shown in Figure 2. We found the work functions of each Pt surface to be similar, validating the use of the Fermi edge as the reference state for the simulated RIXS functions as discussed in S.2.7. Early transition metals such as V and Mn have a well-defined shift in intensity from
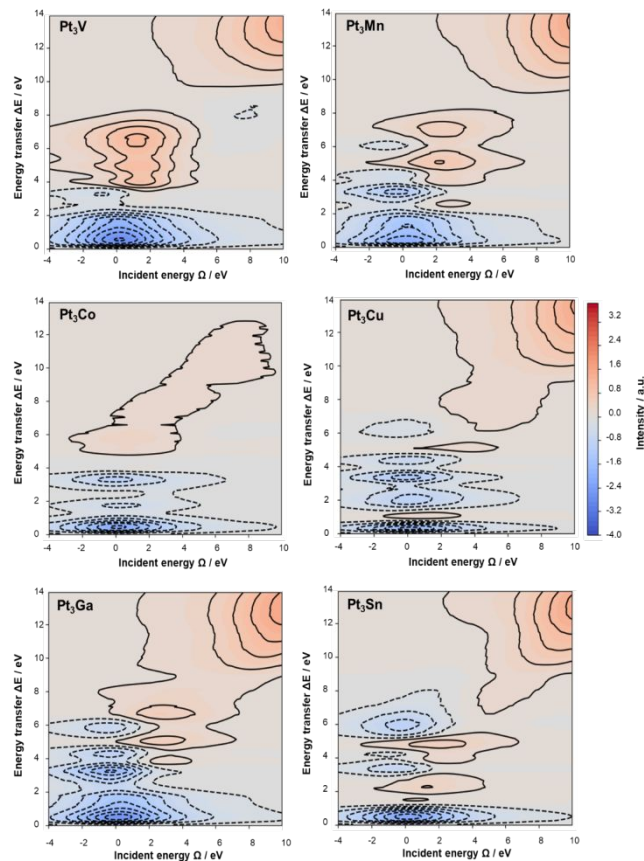
Figure 3. Simulated difference RIXS plots for a subset of the intermetallics. Each plot is shown at 45% dispersion, relative to a similar 45% dispersion pure Pt particle. The 6 other intermetallics considered can be found in the Supplementary information S.3.6.

approximately 0.5 eV incident energy and 0.5 eV energy transfer for Mn to nearly 1.75 eV incident energy and 4 eV energy transfer for V. This contrasts with late transition metals like Co and Cu where the shifts have lower intensity, indicating greater similarity to pure Pt. The shift to higher incident and transfer energies is also observed by late transition metals. The post-transition metals Ga and Sn have more intense transitions than late transition metals, with a shift to higher incident and transfer energies.

Simulated and experimental RIXS spectra for each bimetallic relative to pure Pt were compared according to the shift in high intensity peak for incident energy and energy transfer. These results are shown in Figure 4. The incident energy peak maximum decreases with filling of the d-band up until PtZn where the d-band fills, and the incident energy maxima are larger. PtZn and the post-transition metal promoters Ga and In have similar incident energy maxima, but the incident energy maximum of Sn is lower by nearly 0.4 eV. The agreement with experiment (the mean

absolute error – MAE - of predicted RIXS incident energies is 0.22 eV, with a 0.25 eV MAE for the energy transfer) is quite striking, considering the challenges inherent in convoluting occupied and unoccupied states using GGA level DFT for an excitation process. Some plausible explanations for this agreement are that the RIXS process only includes states close to the Fermi energy, where the one electron GGA wavefunctions are still reasonable, as opposed to simulations of XANES where the inclusion of high energy states causes the one-electron density to fail when electrons localize. In comparison to XPS, core-hole effects are reduced in RIXS simulations, as a valence d-electron fills the core state; so the final state only involves a hole in the valence states as opposed to XPS where the hole is in a core state. Finally, shifts are reported relative to a reference (pure Pt) which may fortuitously cancel some of the intrinsic DFT errors and magnify the more salient structural changes in the d-DOS. Changing particle size from 1.5 nm to 3 nm in the simulations has a relatively small effect in incident energies (largest being Pt$_3$Sn with a size effect of ~0.2 eV), which reflect changes in the d-DOS with dispersion as shown in Figure 2. For RIXS energy transfer, however, the effect of particle dispersion is significantly larger, which as discussed in S.2.8 may be the result of strain in the relative difference between occupied and unoccupied d states.

The strong correlations between experimental and simulated RIXS indicate a deeper connection between spectra and the near-edge Pt d states that govern the transitions. We propose, in turn, that developing correlations between RIXS features and the d band will be useful, because the most successful theories for chemisorption are also related to the d band. One can then envision relating RIXS to chemisorption by using the existing d-band theories as an intermediate descriptor.

We first connect RIXS to the d band theory. To simplify the RIXS analysis, the core-hole broadening term of the RIXS equation was set to unity such that

$$F(\Omega,\omega) = \int_{-\infty}^{0} d\epsilon \frac{\rho_d(\epsilon)\rho_d{'}(\epsilon + \Omega - \omega)}{(\epsilon - \omega)^2 + 1} \qquad (eq\ 1)$$

Where F is the intensity at a given incident (Ω), or emitted
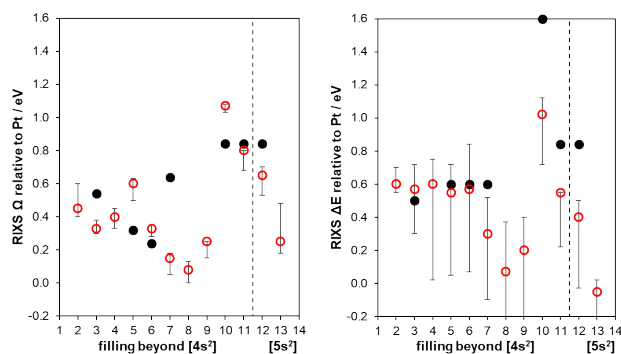
Figure 4. Direct comparison of simulated RIXS spectra from DFT calculated Pt d-DOS (red) and experimental RIXS spectra (black). Error bars correspond to 30%-100% dispersion with 45% dispersion plotted.

(ω) energy. ρ_d are the occupied d states while $\rho_d{'}$ are unoccupied d states. Calculated energy transfer maxima differed on average by 0.02 eV, simplifying the

interpretation but maintaining a similar energy maximum. Changes in the core-hole broadening term; however, change the shape and dispersion of the simulated RIXS distribution, which would be important when fitting parameters away from the maximum value. From inspection of the RIXS equation (eq 1) that includes the convolution of occupied and unoccupied d states, we invoke a similar approximation as the Hammer and Nørskov d-band theory[42,44] by approximating the full range of inter-band interactions by delta functions at the center of the occupied and unoccupied bands (i.e. replacing the full distribution by the occupied and unoccupied d-band centers).

Remarkably, the relative difference between unoccupied and occupied d bands described above is linearly correlated to the RIXS energy transfer feature with a MAE less than 0.1 eV (Figure 5a) for various Pt intermetallics. Thus, the RIXS energy transfer (either

In light alkane dehydrogenation, studies of catalyst deactivation have drawn considerable attention recently[37,58] where the stability of atomic carbon (C), methylidine (CH), and ethylidine (CCH$_3$) have been discussed as the products of C-C bond cleavage in propane dehydrogenation that irreversibly bond to Pt surfaces and result in deactivation.[59] We show that the stability of these coke precursors (CH$_3$, CH$_2$, CH, C, and CCH$_3$) can be predicted using our newly developed RIXS descriptor. As adsorption is a surface process, the approximate nanoparticle models used to find correlations with experimental spectra will be replaced by RIXS spectra of the surface Pt atoms in the alloy, derived from the 100% dispersion DOS in Figure 2. Thus, all d bands and RIXS spectra will be of only surface Pt atoms in the slab.

The relation between the simulated RIXS energy transfer and adsorption is provided in Figure 5b, where strong correlation with the adsorption of carbon
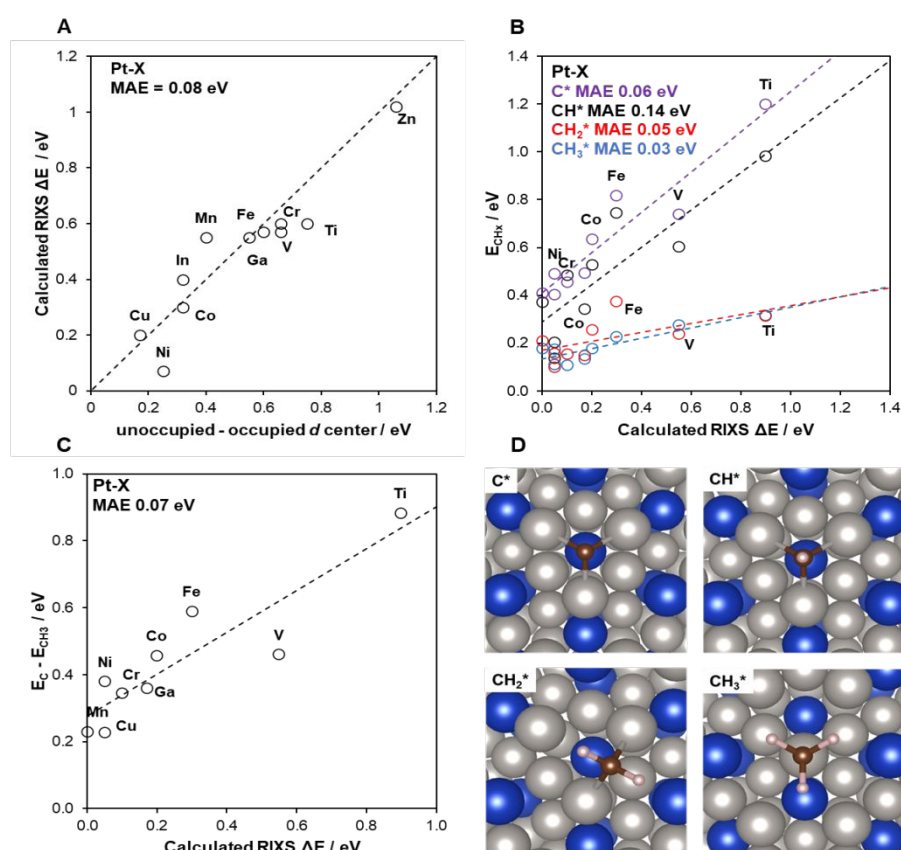
Figure 5. A) Correlation between simulated RIXS energy transfer and d separation descriptor across all 2 nm bimetallic particles relative to pure Pt. B) (C, CH, CH$_2$, CH$_3$) energies, and calculated RIXS ΔE, for the range of Pt-X bimetallics relative to pure Pt. The analysis corresponds to pure surface RIXS (100% dispersion). C) Relative binding energy of C* and CH$_3$*, referenced to pure Pt, for the range of Pt-X bimetallics. D) Representative adsorption sites on a (111) surface. A complete set of images can be found in S.3.8 and S.3.9. Note that PtZn(011) is not included in these correlations, as it has a different composition and surface termination.

simulated or measured), to first order, measures the separation of unoccupied and occupied d states. We can now validate that this new descriptor (unoccupied - occupied d center) also predicts chemisorption. This descriptor is effectively an additional parameter to the traditional d band model, and it is plausible to expect correlations with chemisorption. As a test system, we will consider carbon-containing intermediates relevant to non-oxidative dehydrogenation of alkanes to olefins.

intermediates is observed. The 4d post-transition metal promoters are excluded from this relation, due to their exerted tensile strain; however, Ga has been included. Also, due to its tetragonal unit cell structure, the closest-packed surface for PtZn is (011), where adsorbates have a unique coordination number as compared to the (111) surfaces; so this element is likewise not included in the correlation. The energy transfer predicted for surface In and Sn promoters is negative relative to platinum, -0.07 eV and -0.22 eV,

respectively. This would indicate occupied and unoccupied band centers of these promoters are in fact closer than they are for surface Pt atoms. However, the adsorption of C with In and Sn promoters is weaker than pure Pt, 0.48 eV and 0.96 eV respectively, which cannot be explained by the theories presented here. This discrepancy is likely related to the fact that Sn and In are post-transition metals, and so arguments based on d-band filling and densities of state are not directly applicable. We have examined the effect of strain on the adsorption of each intermediate (S.2.11) indicating that while strain does influence the adsorption of atomic carbon and CH, the predominant effect is electronic. The 4d post-transition promoters are significantly larger than the 3d post-transition metals, and the method of bonding may differ from the 3d metals. We hope this encourages future RIXS studies for the 4d metals. For 3d transition metals and Ga, a visible correlation between calculated RIXS energy transfer and adsorption is apparent. Mean absolute errors are largest for CH (0.14 eV) while the correlation with other adsorbates are on the order of 0.06 eV. The larger errors in CH are due to the influence of oxophilic promoter metals in perturbing adsorption sites. Figure S.3.10. constrains the position of CH for Ti and V promoters to the same sites as the other alloys, which reduces the MAE to 0.10 eV. The adsorption of atomic carbon has been traditionally difficult to predict due to its propensity to form multiple strong bonds to the surface, and we have benchmarked our descriptor against other traditional descriptors, such as the modified d band center (center and width),[60] kurtosis, and skewness, as well as comparisons with the simplified occupied and unoccupied d states and the Hilbert transform maximum.[47] We found the usage of the RIXS convolution has a MAE lower than any of the previous descriptors for atomic carbon (S.2.10).

The RIXS descriptor, in conjunction with scaling relationships[61] and Brønsted-Evans-Polanyi relationships, enable deeper correlations to be established between RIXS and reaction kinetics. Scaling relationships correlate the adsorption energies of similar adsorbates, reducing the space of DFT simulations required to map the energetics of a reaction network. Brønsted-Evans-Polanyi relationships can be combined with scaling relationships to obtain the transition state energies across different catalysts. Because the RIXS descriptor correlates with the adsorption of carbon intermediates, it would be possible in principle to develop a correlation between the RIXS descriptor and a kinetic barrier. We have established scaling relationships between carbon containing intermediates in S.2.11 to demonstrate the scaling facet of these relationships. We can also look at different combinations of these descriptors. For example, the stability of CH_3 groups do not change significantly across the range of promoters examined. More unsaturated intermediates that interact strongly with the surface and subsurface, such as C and CH, have binding energies that vary by up to nearly 1.4 eV in comparison to pure Pt. This dramatic tunability is attractive for catalysis, where in this case we seek to maintain the dehydrogenation rate while preventing deactivation. Regardless of the promoter we choose, the CH_3 adsorption energy, which could be a proxy for the initial CH bond activation in a dehydration mechanism, is not perturbed. We do find, however, that the stability of coke precursors C and CH are significantly affected by the separation of Pt d states. The difference in the adsorption energies of C and CH_3 can be

linearly correlated with the RIXS descriptor (Figure 5c) where catalysts with a larger d separation destabilize C to a greater degree than CH_3. Continuing the example of dehydrogenation, this could manifest as catalysts with greater d separation having a similar dehydrogenation rate as those with less d separation, but a slower C-C scission rate due to the reduced stability of atomic carbon[16].

While the set of adsorbates chosen in this study are limited to single carbon atom intermediates, we can highlight how these relationships are related to larger adsorbates with similar adsorption moieties. Figure S.3.14 describes the relationship between adsorption of CH and CCH_3, both relevant coking precursor molecules.[58] The scaling relationship between these species has a slope of 1, as both molecules bind through a similarly undercoordinated carbon center. All the promoter metals, including the 4d post-transition metals Sn and In, as well as the 1:1 PtZn bimetallic fall on the same relationship, as CH and CCH_3 adsorb at the same sites, producing a constant slope.

The RIXS descriptor has broad applicability because it can be calculated through DFT or measured directly by experiment where the valence electrons involved in catalysis are included. By building the descriptor from the spectroscopy, it is possible to develop structure-function relationships with experimental measurements without the need for calculating parameters with DFT. Of course, measuring RIXS spectra for many catalysts may be intractable, and for high throughput screening a DFT calculated RIXS descriptor would be easier to implement. One could also imagine tiered approaches to catalyst design where first a wide range of bimetallics with different compositions and promoters are explored computationally, and those with larger d separations could be evaluated with experimental measurements, and a final subset of the most promising materials would be subjected to rigorous kinetic and deactivation tests. The internal loop between experimental and simulated RIXS would provide an internal check that simulated materials have physically realizable electronic configurations, which could dramatically reduce the false-positive rate of any exploratory catalyst design project.

Conclusions

The role of promoter metal identity in alloys for heterogeneous catalysis has been a topic of fundamental importance since the work of Sinfelt and coworkers. In this contribution, we have shown how new developments in RIXS spectroscopy have introduced new avenues for understanding how catalyst electronic states are tuned by judicious promoter choice. The specific physics of the spectroscopy, which do not include strong core-hole interactions in the final state, permit DFT theory to develop experimentally accessible catalyst descriptors. We have provided fundamental correlations that relate the measured RIXS energy transfer to moments of the d-band, and then to chemisorption. These simplified d-band moments in the style of Hammer and Nørskov capture the measured shifts, providing a more intuitive understanding of Pt d-state changes. This connection may be especially relevant to studies involving other alloy compositions or promoter identities.

By then correlating this new descriptor with chemisorption, we have shown how the selective destabilization of unsaturated carbon intermediates can be understood as the modulation of *d*-state separation by promoters. This separation is experimentally accessible through RIXS spectroscopy and provides direct comparison with computational studies. By designing descriptors that are connected to experimental measurements, new workflows for catalyst design where theory and characterization are firmly linked using relationships as described herein can be developed to better identify exciting materials with desired chemical properties.

Author Contributions

The manuscript was written through contributions of all authors. All authors have given approval to the final version of the manuscript. ‡These authors contributed equally.

Conflicts of Interest

The authors declare no conflicts of interest.

Present Addresses

Brandon C. Bukowski – Department of Chemical and Biomolecular Engineering, Johns Hopkins University, 3400 North Charles Street, Baltimore MD 21218.

Stephen C. Purdy – Manufacturing Science Division, Oak Ridge National Laboratory, 1 Bethel Valley Road, Oak Ridge TN 37830

Acknowledgements

References

(1)   Kitchin, J. R.; Nørskov, J. K.; Barteau, M. A.; Chen, J. G. Modification of the Surface Electronic and Chemical Properties of Pt(111) by Subsurface 3d Transition Metals. *J. Chem. Phys.* **2004**, *120* (21), 10240–10246. https://doi.org/10.1063/1.1737365.

(2)   Stamenkovic, V. R.; Mun, B. S.; Arenz, M.; Mayrhofer, K. J. J.; Lucas, C. A.; Wang, G.; Ross, P. N.; Markovic, N. M. Trends in Electrocatalysis on Extended and Nanoscale Pt-Bimetallic Alloy Surfaces. *Nature Materials* **2007**, *6* (3), 241–247. https://doi.org/10.1038/nmat1840.

(3)   Humbert, M. P.; Murillo, L. E.; Chen, J. G. Rational Design of Platinum-Based Bimetallic Catalysts with Enhanced Hydrogenation Activity. *ChemPhysChem* **2008**, *9* (9), 1262–1264. https://doi.org/10.1002/cphc.200800139.

(4)   Sun, G.; Zhao, Z.-J.; Mu, R.; Zha, S.; Li, L.; Chen, S.; Zang, K.; Luo, J.; Li, Z.; Purdy, S. C.; Kropf, A. J.; Miller, J. T.; Zeng, L.; Gong, J. Breaking the Scaling Relationship via Thermally Stable Pt/Cu Single Atom Alloys for Catalytic Dehydrogenation. *Nature Communications* **2018**, *9* (1). https://doi.org/10.1038/s41467-018-06967-8.

(5)   Lucci, F. R.; Liu, J.; Marcinkowski, M. D.; Yang, M.; Allard, L. F.; Flytzani-Stephanopoulos, M.; Sykes, E. C. H. Selective Hydrogenation of 1,3-Butadiene on Platinum–Copper Alloys at the Single-Atom Limit. *Nature Communications* **2015**, *6* (1), 8550. https://doi.org/10.1038/ncomms9550.

(6)   Duchesne, P. N.; Li, Z. Y.; Deming, C. P.; Fung, V.; Zhao, X.; Yuan, J.; Regier, T.; Aldalbahi, A.; Almarhoon, Z.; Chen, S.; Jiang, D.; Zheng, N.; Zhang, P. Golden Single-Atomic-Site Platinum Electrocatalysts. *Nature Materials* **2018**, *17* (11), 1033–1039. https://doi.org/10.1038/s41563-018-0167-5.

(7)   Mun, B. S.; Watanabe, M.; Rossi, M.; Stamenkovic, V.; Markovic, N. M.; Ross, P. N. A Study of Electronic Structures of Pt3M (M=Ti,V,Cr,Fe,Co,Ni) Polycrystalline Alloys with Valence-Band Photoemission Spectroscopy. *The Journal of Chemical Physics* **2005**, *123* (20), 204717. https://doi.org/10.1063/1.2126662.

(8)   Lange, K.; Schulz-Ruhtenberg, M.; Caro, J. Platinum Electrodes for Oxygen Reduction Catalysis Designed by Ultrashort Pulse Laser Structuring. *ChemElectroChem* **2017**, *4* (3), 570–576. https://doi.org/10.1002/celc.201600630.

(9)   Xiong, Y.; Yang, Y.; Joress, H.; Padgett, E.; Gupta, U.; Yarlagadda, V.; Agyeman-Budu, D. N.; Huang, X.; Moylan, T. E.; Zeng, R.; Kongkanand, A.; Escobedo, F. A.; Brock, J. D.; DiSalvo, F. J.; Muller, D. A.; Abruña, H. D. Revealing the Atomic Ordering of Binary Intermetallics Using in Situ Heating Techniques at Multilength Scales. *PNAS* **2019**, *116* (6), 1974–1983. https://doi.org/10.1073/pnas.1815643116.

(10)   Ghosh, T.; Leonard, B. M.; Zhou, Q.; DiSalvo, F. J. Pt Alloy and Intermetallic Phases with V, Cr, Mn, Ni, and Cu: Synthesis As Nanomaterials and Possible Applications As Fuel Cell Catalysts. *Chemistry of Materials* **2010**, *22* (7), 2190–2202. https://doi.org/10.1021/cm9018474.

(11)   Armbrüster, M.; Schlögl, R.; Grin, Y. Intermetallic Compounds in Heterogeneous Catalysis—a Quickly Developing Field. *Science and Technology of Advanced Materials* **2014**, *15* (3), 034803. https://doi.org/10.1088/1468-6996/15/3/034803.

(12)   Furukawa, S.; Komatsu, T. Intermetallic Compounds: Promising Inorganic Materials for Well-Structured and Electronically Modified Reaction Environments for Efficient Catalysis. *ACS Catal.* **2017**, *7* (1), 735–765. https://doi.org/10.1021/acscatal.6b02603.

(13)   Cui, Z.; Chen, H.; Zhao, M.; Marshall, D.; Yu, Y.; Abruña, H.; DiSalvo, F. J. Synthesis of Structurally Ordered Pt $_3$ Ti and Pt $_3$ V Nanoparticles as Methanol Oxidation Catalysts.

Journal of the American Chemical Society **2014**, *136* (29), 10206–10209. https://doi.org/10.1021/ja504573a.

(14)   Purdy, S. C.; Ghanekar, P.; Mitchell, G.; Kropf, A. J.; Zemlyanov, D. Y.; Ren, Y.; Ribeiro, F.; Delgass, W. N.; Greeley, J.; Miller, J. T. Origin of Electronic Modification of Platinum in a Pt3V Alloy and Its Consequences for Propane Dehydrogenation Catalysis. *ACS Appl. Energy Mater.* **2020**, *3* (2), 1410–1422. https://doi.org/10.1021/acsaem.9b01373.

(15)   LiBretto, N. J.; Yang, C.; Ren, Y.; Zhang, G.; Miller, J. T. Identification of Surface Structures in Pt3Cr Intermetallic Nanocatalysts. *Chem. Mater.* **2019**, *31* (5), 1597–1609. https://doi.org/10.1021/acs.chemmater.8b04774.

(16)   Wu, Z.; Bukowski, B. C.; Li, Z.; Milligan, C.; Zhou, L.; Ma, T.; Wu, Y.; Ren, Y.; Ribeiro, F. H.; Delgass, W. N.; Greeley, J.; Zhang, G.; Miller, J. T. Changes in Catalytic and Adsorptive Properties of 2 Nm Pt $_3$ Mn Nanoparticles by Subsurface Atoms. *Journal of the American Chemical Society* **2018**, *140* (44), 14870–14877. https://doi.org/10.1021/jacs.8b08162.

(17)   Yu, Z.; Sawada, J. A.; An, W.; Kuznicki, S. M. PtZn-ETS-2: A Novel Catalyst for Ethane Dehydrogenation. *AIChE Journal* **2015**, *61* (12), 4367–4376. https://doi.org/10.1002/aic.15010.

(18)   Cybulskis, V. J.; Bukowski, B. C.; Tseng, H.-T.; Gallagher, J. R.; Wu, Z.; Wegener, E.; Kropf, A. J.; Ravel, B.; Ribeiro, F. H.; Greeley, J.; Miller, J. T. Zinc Promotion of Platinum for Catalytic Light Alkane Dehydrogenation: Insights into Geometric and Electronic Effects. *ACS Catal.* **2017**, *7* (6), 4173–4181. https://doi.org/10.1021/acscatal.6b03603.

(19)   Wegener, E. C.; Bukowski, B. C.; Yang, D.; Wu, Z.; Kropf, A. J.; Delgass, W. N.; Greeley, J.; Zhang, G.; Miller, J. T. Intermetallic Compounds as an Alternative to Single-Atom Alloy Catalysts: Geometric and Electronic Structures from Advanced X-Ray Spectroscopies and Computational Studies. *ChemCatChem* **2020**, *12* (5), 1325–1333. https://doi.org/10.1002/cctc.201901869.

(20)   Furukawa, S.; Tamura, A.; Ozawa, K.; Komatsu, T. Catalytic Properties of Pt-Based Intermetallic Compounds in Dehydrogenation of Cyclohexane and n-Butane. *Applied Catalysis A: General* **2014**, *469*, 300–305. https://doi.org/10.1016/j.apcata.2013.10.012.

(21)   Furukawa, S.; Endo, M.; Komatsu, T. Bifunctional Catalytic System Effective for Oxidative Dehydrogenation of 1-Butene and n-Butane Using Pd-Based Intermetallic Compounds. *ACS Catal.* **2014**, *4* (10), 3533–3542. https://doi.org/10.1021/cs500920p.

(22)   C. Purdy, S.; Rohit Seemakurthi, R.; M. Mitchell, G.; Davidson, M.; A. Lauderback, B.; Deshpande, S.; Wu, Z.; C. Wegener, E.; Greeley, J.; T. Miller, J. Structural Trends in the Dehydrogenation Selectivity of Palladium Alloys. *Chemical Science* **2020**, *11* (19), 5066–5081. https://doi.org/10.1039/D0SC00875C.

(23)   Furukawa, S.; Yoshida, Y.; Komatsu, T. Chemoselective Hydrogenation of Nitrostyrene to Aminostyrene over Pd- and Rh-Based Intermetallic Compounds. *ACS Catal.* **2014**, *4* (5), 1441–1450. https://doi.org/10.1021/cs500082g.

(24)   Maligal-Ganesh, R. V.; Xiao, C.; Goh, T. W.; Wang, L.-L.; Gustafson, J.; Pei, Y.; Qi, Z.; Johnson, D. D.; Zhang, S.; Tao, F. (Feng); Huang, W. A Ship-in-a-Bottle Strategy To Synthesize Encapsulated Intermetallic Nanoparticle Catalysts: Exemplified for Furfural Hydrogenation. *ACS Catal.* **2016**, *6* (3), 1754–1763. https://doi.org/10.1021/acscatal.5b02281.

(25)   Ota, A.; Armbrüster, M.; Behrens, M.; Rosenthal, D.; Friedrich, M.; Kasatkin, I.; Girgsdies, F.; Zhang, W.; Wagner, R.; Schlögl, R. Intermetallic Compound Pd2Ga as a Selective Catalyst for the Semi-Hydrogenation of Acetylene: From Model to High Performance Systems. *J. Phys. Chem. C* **2011**, *115* (4), 1368–1374. https://doi.org/10.1021/jp109226r.

(26)   Elattar, A.; Takeshita, T.; Wallace, W. E.; Craig, R. S. Intermetallic Compounds of the Type MNi5 as Methanation Catalysts. *Science* **1977**, *196* (4294), 1093–1094. https://doi.org/10.1126/science.196.4294.1093.

(27)   Luengo, C. A.; Cabrera, A. L.; MacKay, H. B.; Maple, M. B. Catalysis of Carbon Monoxide and Carbon Dioxide Methanation by CeAl2, CeCo2, CeNi2, Co, and Ni. *Journal of Catalysis* **1977**, *47* (1), 1–10. https://doi.org/10.1016/0021-9517(77)90144-0.

(28)   Siirola, J. J. The Impact of Shale Gas in the Chemical Industry. *AIChE Journal* **2014**, *60* (3), 810–819. https://doi.org/10.1002/aic.14368.

(29)   Al-Douri, A.; Sengupta, D.; El-Halwagi, M. M. Shale Gas Monetization – A Review of Downstream Processing to Chemicals and Fuels. *Journal of Natural Gas Science and Engineering* **2017**, *45*, 436–455. https://doi.org/10.1016/j.jngse.2017.05.016.

(30)   Sinfelt, J. H. Catalysis by Alloys and Bimetallic Clusters. *Acc. Chem. Res.* **1977**, *10* (1), 15–20. https://doi.org/10.1021/ar50109a003.

(31)   Sinfelt, J. H.; Carter, J. L.; Yates, D. J. C. Catalytic Hydrogenolysis and Dehydrogenation over Copper-Nickel Alloys. *Journal of Catalysis* **1972**, *24* (2), 283–296. https://doi.org/10.1016/0021-9517(72)90072-3.

(32)   Sattler, J. J. H. B.; Ruiz-Martinez, J.; Santillan-Jimenez, E.; Weckhuysen, B. M. Catalytic Dehydrogenation of Light Alkanes on Metals and Metal Oxides. *Chem. Rev.* **2014**, *114* (20), 10613–10653. https://doi.org/10.1021/cr5002436.

(33)   Guisnet, M.; Magnoux, P. Organic Chemistry of Coke Formation. *Applied Catalysis A: General* **2001**, *212* (1), 83–96. https://doi.org/10.1016/S0926-860X(00)00845-0.

(34)   Bariås, O. A.; Holmen, A.; Blekkan, E. A. Propane Dehydrogenation over Supported Pt and Pt–Sn Catalysts: Catalyst Preparation, Characterization, and Activity Measurements. *Journal of Catalysis* **1996**, *158* (1), 1–12. https://doi.org/10.1006/jcat.1996.0001.

(35)   Kappenstein, C.; Gue′rin, M.; Lázár, K.; Matusek, K.; Paál, Z. Characterisation and Activity in N-Hexane Rearrangement Reactions of Metallic Phases on Pt–Sn/Al2O3 Catalysts of Different Preparations. *J. Chem. Soc., Faraday Trans.* **1998**, *94* (16), 2463–2473. https://doi.org/10.1039/A803014F.

(36)   Santhosh Kumar, M.; Chen, D.; Holmen, A.; Walmsley, J. C. Dehydrogenation of Propane over Pt-SBA-15 and Pt-Sn-SBA-15: Effect of Sn on the Dispersion of Pt and Catalytic Behavior. *Catalysis Today* **2009**, *142* (1), 17–23. https://doi.org/10.1016/j.cattod.2009.01.002.

(37)   Nykänen, L.; Honkala, K. Selectivity in Propene Dehydrogenation on Pt and Pt $_3$ Sn Surfaces from First Principles. *ACS Catalysis* **2013**, *3* (12), 3026–3030. https://doi.org/10.1021/cs400566y.

(38)   Nykänen, L.; Honkala, K. Density Functional Theory Study on Propane and Propene Adsorption on Pt(111) and PtSn Alloy Surfaces. *The Journal of Physical Chemistry C* **2011**, *115* (19), 9578–9586. https://doi.org/10.1021/jp1121799.

(39)   Li, H.; Shin, K.; Henkelman, G. Effects of Ensembles, Ligand, and Strain on Adsorbate Binding to Alloy Surfaces. *J. Chem. Phys.* **2018**, *149* (17), 174705. https://doi.org/10.1063/1.5053894.

(40)   Jo, D. Y.; Lee, M. W.; Kim, C. H.; Choung, J. W.; Ham, H. C.; Lee, K.-Y. Interplay of Ligand and Strain Effects in CO Adsorption on Bimetallic Cu/M (M = Ni, Ir, Pd, and Pt) Catalysts from First-Principles: Effect of Different Facets on Catalysis. *Catalysis Today* **2019**. https://doi.org/10.1016/j.cattod.2019.05.031.

(41)   Greiner, M. T.; Jones, T. E.; Beeg, S.; Zwiener, L.; Scherzer, M.; Girgsdies, F.; Piccinin, S.; Armbrüster, M.; Knop-Gericke, A.; Schlögl, R. Free-Atom-like d States in Single-Atom Alloy Catalysts. *Nature Chemistry* **2018**, *10* (10), 1008–1015. https://doi.org/10.1038/s41557-018-0125-5.

(42)   Hammer, B.; Nørskov, J. K. Electronic Factors Determining the Reactivity of Metal Surfaces. *Surface Science* **1995**, *343* (3), 211–220. https://doi.org/10.1016/0039-6028(96)80007-0.

(43)   Hammer, B.; Nørskov, J. K. Theoretical Surface Science and Catalysis—Calculations and Concepts. In *Advances in Catalysis*; Elsevier, 2000; Vol. 45, pp 71–129. https://doi.org/10.1016/S0360-0564(02)45013-4.

(44)   Hammer, B.; Norskov, J. K. Why Gold Is the Noblest of All the Metals. *Nature* **1995**, *376* (6537), 238. https://doi.org/10.1038/376238a0.

(45)   Nørskov, J. K.; Bligaard, T.; Logadottir, A.; Bahn, S.; Hansen, L. B.; Bollinger, M.; Bengaard, H.; Hammer, B.; Sljivancanin, Z.; Mavrikakis, M.; Xu, Y.; Dahl, S.; Jacobsen, C. J. H. Universality in Heterogeneous Catalysis. *Journal of Catalysis* **2002**, *209* (2), 275–278. https://doi.org/10.1006/jcat.2002.3615.

(46)   Newns, D. M. Self-Consistent Model of Hydrogen Chemisorption. *Physical Review* **1969**, *178* (3), 1123–1135. https://doi.org/10.1103/PhysRev.178.1123.

(47)   Xin, H.; Vojvodic, A.; Voss, J.; Nørskov, J. K.; Abild-Pedersen, F. Effects of d-Band Shape on the Surface Reactivity of Transition-Metal Alloys. *Phys. Rev. B* **2014**, *89* (11), 115114. https://doi.org/10.1103/PhysRevB.89.115114.

(48)   Höchst, H.; Hüfner, S.; Goldmann, A. XPS-Valence Bands of Iron, Cobalt, Palladium and Platinum. *Physics Letters A* **1976**, *57* (3), 265–266. https://doi.org/10.1016/0375-9601(76)90059-1.

(49)   Kotani, A.; Shin, S. Resonant Inelastic X-Ray Scattering Spectra for Electrons in Solids. *Rev. Mod. Phys.* **2001**, *73* (1), 203–246. https://doi.org/10.1103/RevModPhys.73.203.

(50)   Ament, L. J. P.; van Veenendaal, M.; Devereaux, T. P.; Hill, J. P.; van den Brink, J. Resonant Inelastic X-Ray Scattering Studies of Elementary Excitations. *Rev. Mod. Phys.* **2011**, *83* (2), 705–767. https://doi.org/10.1103/RevModPhys.83.705.

(51)   Singh, J.; Lamberti, C.; Bokhoven, J. A. van. Advanced X-Ray Absorption and Emission Spectroscopy: In Situ Catalytic Studies. *Chem. Soc. Rev.* **2010**, *39* (12), 4754–4766. https://doi.org/10.1039/C0CS00054J.

(52)   Glatzel, P.; Singh, J.; Kvashnina, K. O.; van Bokhoven, J. A. In Situ Characterization of the 5d Density of States of Pt Nanoparticles upon Adsorption of CO. *J. Am. Chem. Soc.* **2010**, *132* (8), 2555–2557. https://doi.org/10.1021/ja907760p.

(53)   Singh, J.; Nelson, R. C.; Vicente, B. C.; Scott, S. L.; Bokhoven, J. A. van. Electronic Structure of Alumina-Supported Monometallic Pt and Bimetallic PtSn Catalysts under Hydrogen and Carbon Monoxide Environment. *Phys.*

Chem. Chem. Phys. **2010**, *12* (21), 5668–5677. https://doi.org/10.1039/C000403K.

(54)   Suljoti, E.; Garcia-Diez, R.; Bokarev, S. I.; Lange, K. M.; Schoch, R.; Dierker, B.; Dantz, M.; Yamamoto, K.; Engel, N.; Atak, K.; Kühn, O.; Bauer, M.; Rubensson, J.-E.; Aziz, E. F. Direct Observation of Molecular Orbital Mixing in a Solvated Organometallic Complex. *Angew. Chem. Int. Ed.* **2013**, *52* (37), 9841–9844. https://doi.org/10.1002/anie.201303310.

(55)   Yan, J. J.; Kroll, T.; Baker, M. L.; Wilson, S. A.; Decréau, R.; Lundberg, M.; Sokaras, D.; Glatzel, P.; Hedman, B.; Hodgson, K. O.; Solomon, E. I. Resonant Inelastic X-Ray Scattering Determination of the Electronic Structure of Oxyhemoglobin and Its Model Complex. *PNAS* **2019**, 201815981. https://doi.org/10.1073/pnas.1815981116.

(56)   Cesar, L. G.; Yang, C.; Lu, Z.; Ren, Y.; Zhang, G.; Miller, J. T. Identification of a Pt$_3$Co Surface Intermetallic Alloy in Pt–Co Propane Dehydrogenation Catalysts. *ACS Catal.* **2019**, 5231–5244. https://doi.org/10.1021/acscatal.9b00549.

(57)   Wegener, E. C.; Wu, Z.; Tseng, H.-T.; Gallagher, J. R.; Ren, Y.; Diaz, R. E.; Ribeiro, F. H.; Miller, J. T. Structure and Reactivity of Pt–In Intermetallic Alloy Nanoparticles: Highly Selective Catalysts for Ethane Dehydrogenation. *Catalysis Today* **2018**, *299*, 146–153. https://doi.org/10.1016/j.cattod.2017.03.054.

(58)   Saerens, S.; Sabbe, M. K.; Galvita, V. V.; Redekop, E. A.; Reyniers, M.-F.; Marin, G. B. The Positive Role of Hydrogen on the Dehydrogenation of Propane on Pt(111). *ACS Catal.* **2017**, *7* (11), 7495–7508. https://doi.org/10.1021/acscatal.7b01584.

(59)   Seemakurthi, R. R.; Canning, G.; Wu, Z.; Miller, J. T.; Datye, A. K.; Greeley, J. Identification of a Selectivity Descriptor for Propane Dehydrogenation through Density Functional and Microkinetic Analysis on Pure Pd and Pd Alloys. *ACS Catal.* **2021**, *11* (15), 9588–9604. https://doi.org/10.1021/acscatal.1c01916.

(60)   Vojvodic, A.; Nørskov, J. K.; Abild-Pedersen, F. Electronic Structure Effects in Transition Metal Surface Chemistry. *Top Catal* **2014**, *57* (1), 25–32. https://doi.org/10.1007/s11244-013-0159-2.

(61)   Abild-Pedersen, F.; Greeley, J.; Studt, F.; Rossmeisl, J.; Munter, T. R.; Moses, P. G.; Skúlason, E.; Bligaard, T.; Nørskov, J. K. Scaling Properties of Adsorption Energies for Hydrogen-Containing Molecules on Transition-Metal Surfaces. *Phys. Rev. Lett.* **2007**, *99* (1), 016105. https://doi.org/10.1103/PhysRevLett.99.016105.

(62)   Bolin, T. B.; Wu, T.; Schweitzer, N.; Lobo-Lapidus, R.; Kropf, A. J.; Wang, H.; Hu, Y.; Miller, J. T.; Heald, S. M. In Situ Intermediate-Energy X-Ray Catalysis Research at the Advanced Photon Source Beamline 9-BM. *Catalysis Today* **2013**, *205*, 141–147. https://doi.org/10.1016/j.cattod.2012.09.034.

(63)   Kraft, S.; Stümpel, J.; Becker, P.; Kuetgens, U. High Resolution X-ray Absorption Spectroscopy with Absolute Energy Calibration for the Determination of Absorption Edge Energies. *Review of Scientific Instruments* **1996**, *67* (3), 681–687. https://doi.org/10.1063/1.1146657.

(64)   Ravel, B.; Kropf, A. J.; Yang, D.; Wang, M.; Topsakal, M.; Lu, D.; Stennett, M. C.; Hyatt, N. C. Nonresonant Valence-to-Core x-Ray Emission Spectroscopy of Niobium. *Physical Review B* **2018**, *97* (12), 125139. https://doi.org/10.1103/PhysRevB.97.125139.

(65)   Bradley, L.; Sipőcz, B.; Robitaille, T.; Tollerud, E.; Vinícius, Z.; Deil, C.; Barbary, K.; Wilson, T. J.; Busko, I.; Donath, A.; Günther, H. M.; Cara, M.; Lim, P. L.; Meßlinger, S.;

Conseil, S.; Bostroem, A.; Droettboom, M.; Bray, E. M.; Bratholm, L. A.; Barentsen, G.; Craig, M.; Rathi, S.; Pascual, S.; Perren, G.; Georgiev, I. Y.; Val-Borro, M. de; Kerzendorf, W.; Bach, Y. P.; Quint, B.; Souchereau, H. Astropy/Photutils: 1.5.0, 2022. https://doi.org/10.5281/zenodo.6825092.

(66)   Kresse, G.; Furthmüller, J. Efficiency of Ab-Initio Total Energy Calculations for Metals and Semiconductors Using a Plane-Wave Basis Set. *Computational Materials Science* **1996**, *6* (1), 15–50. https://doi.org/10.1016/0927-0256(96)00008-0.

(67)   Kresse, G.; Furthmüller, J. Efficient Iterative Schemes for \textit{ab Initio} Total-Energy Calculations Using a Plane-Wave Basis Set. *Phys. Rev. B* **1996**, *54* (16), 11169–11186. https://doi.org/10.1103/PhysRevB.54.11169.

(68)   Kresse, G.; Hafner, J. \textit{Ab Initio} Molecular Dynamics for Liquid Metals. *Phys. Rev. B* **1993**, *47* (1), 558–561. https://doi.org/10.1103/PhysRevB.47.558.

(69)   Kresse, G.; Hafner, J. \textit{Ab Initio} Molecular-Dynamics Simulation of the Liquid-Metal\char21{}amorphous-Semiconductor Transition in Germanium. *Phys. Rev. B* **1994**, *49* (20), 14251–14269. https://doi.org/10.1103/PhysRevB.49.14251.

(70)   Kresse, G.; Joubert, D. From Ultrasoft Pseudopotentials to the Projector Augmented-Wave Method. *Phys. Rev. B* **1999**, *59* (3), 1758–1775. https://doi.org/10.1103/PhysRevB.59.1758.

(71)   Blöchl, P. E. Projector Augmented-Wave Method. *Phys. Rev. B* **1994**, *50* (24), 17953–17979. https://doi.org/10.1103/PhysRevB.50.17953.

(72)   Perdew, J. P.; Burke, K.; Ernzerhof, M. Generalized Gradient Approximation Made Simple. *Phys. Rev. Lett.* **1996**, *77* (18), 3865–3868. https://doi.org/10.1103/PhysRevLett.77.3865.

(73)   Wellendorff, J.; Silbaugh, T. L.; Garcia-Pintos, D.; Nørskov, J. K.; Bligaard, T.; Studt, F.; Campbell, C. T. A Benchmark Database for Adsorption Bond Energies to Transition Metal Surfaces and Comparison to Selected DFT Functionals. *Surface Science* **2015**, *640*, 36–44. https://doi.org/10.1016/j.susc.2015.03.023.

(74)   Boudart, M. *Kinetics of Heterogeneous Catalytic Reactions.*; Princeton Univ Press: Place of publication not identified, 2014.